

An orbital water-ice cycle on comet 67P from colour changes

<https://doi.org/10.1038/s41586-020-1960-2>

Received: 5 August 2019

Accepted: 5 November 2019

Published online: 5 February 2020

Gianrico Filacchione^{1*}, Fabrizio Capaccioni¹, Mauro Ciarniello¹, Andrea Raponi¹, Giovanna Rinaldi¹, Maria Cristina De Sanctis¹, Dominique Bockelée-Morvan², Stéphane Erard², Gabriele Arnold³, Vito Mennella⁴, Michelangelo Formisano¹, Andrea Longobardo¹ & Stefano Mottola³

Solar heating of a cometary surface provides the energy necessary to sustain gaseous activity, through which dust is removed^{1,2}. In this dynamical environment, both the coma^{3,4} and the nucleus^{5,6} evolve during the orbit, changing their physical and compositional properties. The environment around an active nucleus is populated by dust grains with complex and variegated shapes⁷, lifted and diffused by gases freed from the sublimation of surface ices^{8,9}. The visible colour of dust particles is highly variable: carbonaceous organic material-rich grains¹⁰ appear red while magnesium silicate-rich^{11,12} and water-ice-rich^{13,14} grains appear blue, with some dependence on grain size distribution, viewing geometry, activity level and comet family type. We know that local colour changes are associated with grain size variations, such as in the bluer jets made of submicrometre grains on comet Hale–Bopp¹⁵ or in the fragmented grains in the coma¹⁶ of C/1999 S4 (LINEAR). Apart from grain size, composition also influences the coma's colour response, because transparent volatiles can introduce a substantial blueing in scattered light, as observed in the dust particles ejected after the collision of the Deep Impact probe with comet 9P/Tempel 1¹⁷. Here we report observations of two opposite seasonal colour cycles in the coma and on the surface of comet 67P/Churyumov–Gerasimenko through its perihelion passage¹⁸. Spectral analysis indicates an enrichment of submicrometre grains made of organic material and amorphous carbon in the coma, causing reddening during the passage. At the same time, the progressive removal of dust from the nucleus causes the exposure of more pristine and bluish icy layers on the surface. Far from the Sun, we find that the abundance of water ice on the nucleus is reduced owing to redeposition of dust and dehydration of the surface layer while the coma becomes less red.

Understanding how comets work and evolve is one of the most compelling questions to which the Rosetta mission¹⁸ has been trying to find an answer. Unlike past fly-by missions to comets, Rosetta was designed to enter the same orbit and accompany comet 67P/Churyumov–Gerasimenko (hereafter 67P) through its perihelion passage, giving us the unique opportunity to follow the colour changes developing on a comet nucleus and coma in its active phase through the inner Solar System. So far, several studies have investigated how dust and gas (H₂O, CO₂) production³ are correlated during one cometary rotation, showing that the water-ice sublimation on the surface of 67P is the driving mechanism for dust ejection in the coma². In fact, the dust emission flux appears lower above high-cohesion consolidated terrains and reaches a maximum when the subsolar direction is aligned above volatile-rich areas. As the illumination conditions continuously change on 67P, rather than focusing on coma and nucleus colour variations occurring during a few diurnal rotations, we analysed the entire dataset

returned by the Visible, Infrared and Thermal Imaging Spectrometer (VIRTIS)¹⁹ on Rosetta. Our method allows exploration of the comet's colour evolution starting from January 2015 (inbound orbit, heliocentric distance 2.55 AU), encompassing perihelion passage (August 2015, 1.24 AU) until May 2016 (outbound orbit, 2.92 AU). Spectral indicators in the visible range, including the integrated radiance (*I*), the wavelength of the radiance peak (λ_{max}) and the spectral slopes (in the 0.4–0.5 and 0.5–0.8 μm ranges), are synergistically used to model the composition and grain size distribution of the dust particles in the coma as a function of heliocentric distance. The spectral indicators are derived for each spectrum acquired by VIRTIS in an annulus encircling the nucleus and comprising all the pixels in the coma located at a tangent altitude between 1.0 and 2.5 km above the nucleus' limb. At the same time, we monitor the colour changes occurring on 12 test areas on the nucleus through the 0.5–0.8 μm spectral slope^{5,6}. The description of the dataset, including an example of VIRTIS images and spectra after calibration

¹INAF-IAPS, Institute for Space Astrophysics and Planetology, Rome, Italy. ²LESIA, Observatoire de Paris, Université PSL, CNRS, Sorbonne Université, Université Paris Diderot Sorbonne Paris Cité, Meudon, France. ³German Aerospace Center (DLR), Institute of Planetary Research, Berlin, Germany. ⁴INAF—Osservatorio Astronomico di Capodimonte, Naples, Italy. *e-mail: gianrico.filacchione@inaf.it

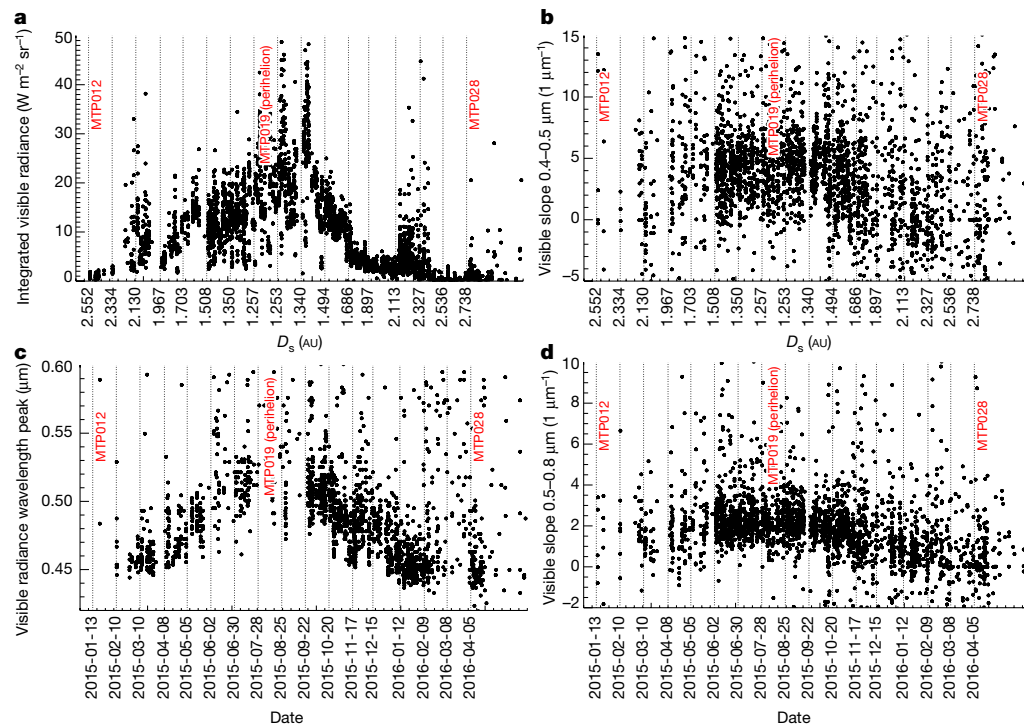


Fig. 1 | Time series of the spectral properties of 67P coma dust. **a**, Integrated radiance (I); full dataset, partial annulus coverage (black points); reduced dataset, complete annulus coverage (red points; see discussion in Methods). **b**, The 0.4–0.5 μm spectral slope. **c**, Visible radiance wavelength peak λ_{max} . **d**, The 0.5–0.8 μm spectral slope. Throughout the paper, spectral slopes are given in μm^{-1} corresponding to 10%/100 nm colour slope. Rosetta's MTP intervals are marked by vertical lines between MTP012 and MTP028. Time intervals and heliocentric distance (D_s) of MTP periods are listed in Extended Data Table 1. Perihelion occurs during MTP019. Dates are displayed as year-month-day.

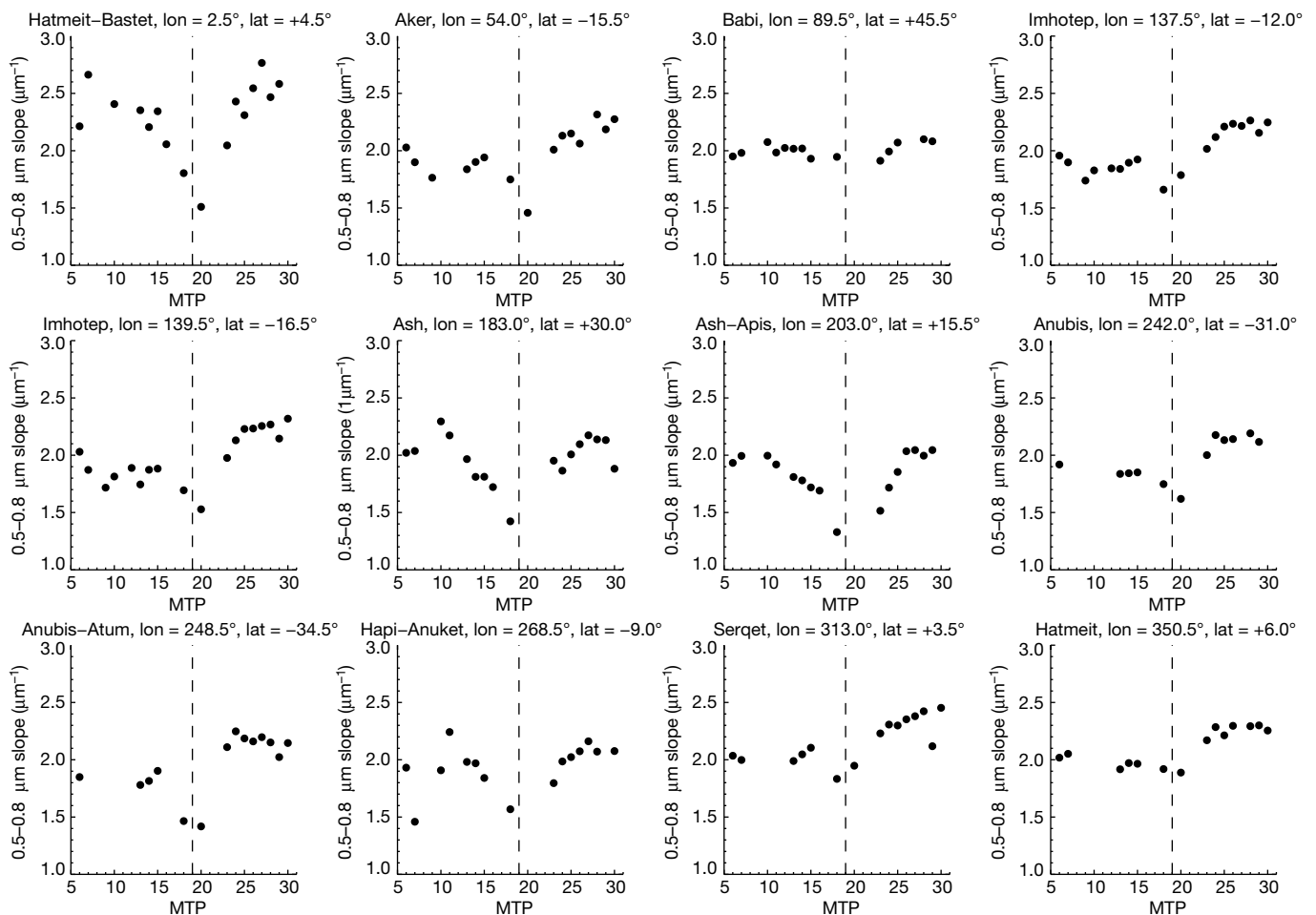


Fig. 2 | Time evolution of 67P nucleus colour measured through the 0.5–0.8 μm spectral slope above 12 control areas. Perihelion passage occurs during MTP019 and is marked by the vertical dashed line. The morphological

region name and position (longitude, lon, and latitude, lat) of each area are reported above each plot. The maximum error associated with the slope measurements is of the order of $\pm 0.1 \mu\text{m}^{-1}$.

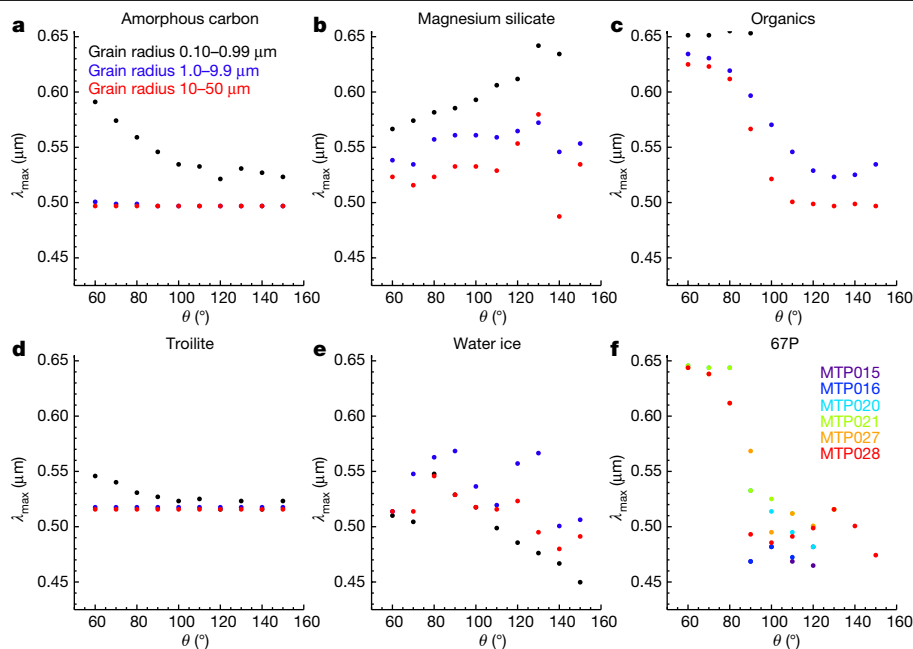


Fig. 3 | Simulations of the λ_{max} as a function of the scattering angle for spherical particles of different composition. a, Amorphous carbon. b, Magnesium silicate. c, Organic ice tholin ($\lambda_{\text{max}} > 0.65 \mu\text{m}$ for 0.10–0.99- μm -radius grains). d, Troilite. e, Water ice. f, 67P observations by VIRTIS. Median

data computed on 10° bin scattering angles (θ) during different mission phases. Standard deviation computed on VIRTIS data are of the order of $0.03 \mu\text{m}$.

improvement, spectral indicator processing and data modelling, are given in Methods.

From a synergistic time analysis of the coma and of the nucleus surface spectral properties, two opposite trends with heliocentric distance are observed. Coma integrated radiance increases (see I time series in Fig. 1a) and colour becomes redder when the comet approaches perihelion (see time series of λ_{max} and the 0.4–0.5 and 0.5–0.8 μm spectral slopes in Fig. 1b–d). Conversely, on 12 control areas of the nucleus, for which we have continuous time coverage during the entire Rosetta mission, we observe a systematic blueing of the surface (see 0.5–0.8 μm spectral slope time series in Fig. 2), with a reduction of the spectral slope up to 50% measured between the passage of 67P through the frost line (heliocentric distance 2.7 AU, occurring in October 2014 during inbound orbit and in April 2016 on the outbound) and perihelion (1.25 AU, August 2015). During the pre-perihelion period, we interpret the coma colour change as being the consequence of the progressive loss of the ice fraction in the dust grains ejected from the nucleus²⁰, which makes them redder.

When the comet approaches the Sun, the dust grains lifted from the nucleus' southern hemisphere—the one illuminated at that time—are warmer and become more dehydrated. Simulations based on Mie scattering theory applied to spherical grains of radius between 0.1 and 50 μm and five different compositions (see Methods for a discussion about the scattering model limitations induced by spherical shaped grains) are used to model VIRTIS spectral indicators, for example, λ_{max} and the 0.5–0.8 μm spectral slope. Simulation results (Figs. 3, 4) are compatible with the presence of submicrometre grains made of organic matter and carbon during perihelion passage, which could be the result of the fragmentation of the mineral and organic matrix embedded in larger grains. During the outbound orbit, the simulations show that the organic material continues to be present in the coma together with an increasing percentage of different grains (water ice or magnesium silicate, both of which are not fully compatible with the spectral indicator trends (Extended Data Table 3)), contributing to the progressive blueing observed in the data. In this orbital phase, the Sun shines again on the northern hemisphere, from where a greater flux of surficial water-ice-rich grains²¹ is lifted in the coma.

Conversely, the nucleus' surface becomes progressively bluer during the inbound orbit because the greater solar input causes an increase in the gaseous activity. This triggers dust ejection with consequent erosion of the surface: on average, a 0.5-m-thick erosion layer is lost during each orbit²¹. As a result of this process, more pristine subsurface layers enriched in water ice are exposed on the surface, which turns bluer^{5,6,22}. We have evidence⁶, in fact, that water-ice-rich layers are immediately available under the dust layer, as shown in areas of recent disruption of the surface²³ and as demonstrated by many thermal models applied to cometary nuclei^{24,25}. Between 20% (ref. ²¹) and 50% (ref. ²⁶) of the dust grains ejected around perihelion from the south pole—the region that receives the maximum insolation at that time—fall back preferentially on the northern hemisphere. The fall-back flux is dominated by decimetre-size dust aggregates in which a small fraction of water ice can be maintained²¹. After perihelion, as soon as activity begins to settle, the progressive accumulation of dust on the surface covers the exposed pristine layers again, making the nucleus surface redder again. This process explains the colour cycle observed by VIRTIS on the nucleus (Fig. 2).

The colour of the 67P coma particles can be modelled with different grain populations made of water ice before perihelion, organic material and carbon at perihelion, and water ice or possibly magnesium silicate after perihelion. Similar composition endmembers are compatible with the findings reported by previous Rosetta studies: during outbursts, the release of submicrometre-size water-ice grains mixed with hundred-micrometre-size refractory grains has been observed²⁷. At the same time, a broad emission feature between 3.4 and 3.6 μm has been detected by VIRTIS²⁸, which is compatible with the sublimation of organic materials caused by the high temperatures of the grains. The colour reduction observed when the comet was far from the Sun resembles the spectral properties of water-ice grains, whose existence in the lower coma has been confirmed by other investigations: apart from the presence of submicrometre-size water-ice grains ejected during outbursts²⁷, thermal models and Optical, Spectroscopic, and Infrared Remote Imaging System (OSIRIS) camera images²⁰ show that at 1.53 AU heliocentric distance, the total sublimation of ice for grains of

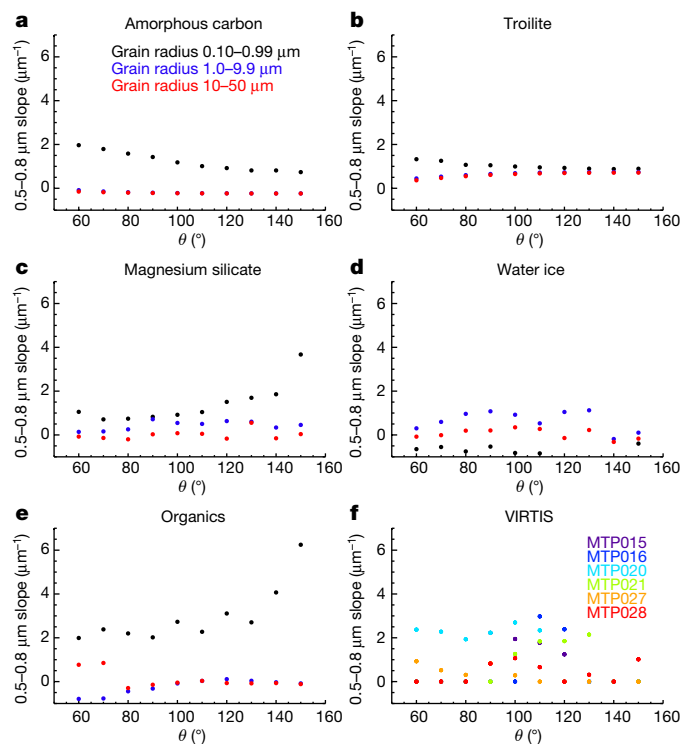


Fig. 4 | Simulations of the 0.5–0.8 μm spectral slope as a function of the scattering angle for spherical particles of different composition. **a, Amorphous carbon. **b**, Troilite. **c**, Magnesium silicate. **d**, Water ice. **e**, Organics. **f**, Median spectral slope derived from VIRTIS observations for pre-perihelion (MTP015 and MTP016), perihelion (MTP020 and MTP021) and post-perihelion (MTP027 and MTP028) mission phases. The standard deviations of the VIRTIS data are $\leq 0.6 \mu\text{m}^{-1}$.**

radius between 5 and 500 μm made of ice-dust layers or mixtures occurs well beyond the 2.5 km distance from the 67P nucleus considered here. This implies that water-ice grains can populate the region of the coma analysed in this study. Finally, a photometric investigation of the visible colours of more than 1,000 individual grains resolved on OSIRIS colour images of the 67P coma²⁹ indicates the presence of three composition classes: organic material grains (steep colour slope), mixtures of silicate and organic material (intermediate slope), and water ice (flat slope). The presence of carbon, silicates and magnesium in 67P dust grains has been assessed by the Cometary Secondary Ion Mass Analyser (COSIMA) instrument on Rosetta³⁰.

The fact that the coma's and the surface's colour spectral indicators return to the same values at the beginning and at the end of their time series (Fig. 1), for example, at heliocentric distances greater than 2.7 AU, is evidence of the establishment of an orbital water-ice cycle driven by the solar heating. Far from the Sun, with the settling down of the gaseous activity³, a tenuous ($I \approx 0$ in Fig. 1a) coma surrounds a red-coloured dusty nucleus.

Online content

Any methods, additional references, Nature Research reporting summaries, source data, extended data, supplementary information,

acknowledgements, peer review information; details of author contributions and competing interests; and statements of data and code availability are available at <https://doi.org/10.1038/s41586-020-1960-2>.

- Gundlach, B., Blum, J., Keller, H. U. & Skorov, Y. V. What drives the dust activity of comet 67P/Churyumov-Gerasimenko? *Astron. Astrophys.* **583**, A12 (2015).
- Tubiana, C. et al. Diurnal variation of dust and gas production in comet 67P/Churyumov-Gerasimenko at the inbound equinox as seen by OSIRIS and VIRTIS-M on board Rosetta. *Astron. Astrophys.* **630**, A23 (2019).
- Hansen, K. C. et al. Evolution of water production of 67P/Churyumov-Gerasimenko: an empirical model and a multi-instrument study. *Mon. Not. R. Astron. Soc.* **462**, S491–S506 (2016).
- Bockelée-Morvan, D. et al. VIRTIS-H observations of comet 67P's dust coma: spectral properties and color temperature variability with phase and elevation. *Astron. Astrophys.* **630**, A22 (2019).
- Filacchione, G. et al. The global surface composition of 67P/CG nucleus by Rosetta/VIRTIS. (I) Prelanding mission phase. *Icarus* **274**, 334–349 (2016).
- Ciarniello, M. et al. The global surface composition of 67P/Churyumov-Gerasimenko nucleus by Rosetta/VIRTIS. (II) Diurnal and seasonal variability. *Mon. Not. R. Astron. Soc.* **462**, S443–S458 (2016).
- Güttler, C. et al. Synthesis of the morphological description of cometary dust at comet 67P. *Astron. Astrophys.* **630**, A24 (2019).
- Huebner, W. F. et al. (eds) *Heat and Gas Diffusion in Comet Nuclei*, SR-004, June, 2006 (ESA Publications Division, 2006).
- Lauter, M. et al. Surface localization of gas sources on comet 67P/Churyumov-Gerasimenko based on DFMS/COPS data. *Mon. Not. R. Astron. Soc.* **483**, 852–861 (2019).
- Jewitt, D. & Meech, K. J. Cometary grain scattering versus wavelength, or, "What color is comet dust?" *Astron. Astrophys. J.* **310**, 937–952 (1986).
- Zubko, E. et al. Interpretation of photopolarimetric observations of comet 17P/Holmes. *J. Quant. Spectrosc. Radiat. Transf.* **112**, 1848–1863 (2011).
- Hadamcik, E. et al. Linear polarization of light scattered by cometary analogs: new samples in *Asteroids, Comets and Meteors 2014* (eds Muinonen, K. et al.) (2014).
- Beer, E. in *Deep Impact as a World Observatory Event: Synergies in Space, Time and Wavelengths* (eds Käufel, H. U. & Sterken, C.) 59–67 (Springer, 2009).
- Fernández, Y. R. et al. Near-infrared light curve of comet 9P/Tempel 1 during Deep Impact. *Icarus* **187**, 220–227 (2007).
- Furusho, R. et al. Imaging polarimetry and color of the inner coma of comet Hale-Bopp (C/1995 O1). *Publ. Astron. Soc. Jpn* **51**, 367–373 (1999).
- Hadamcik, E. & Levasseur-Regourd, A. C. Dust coma of comet C/1999 S4 (LINEAR): imaging polarimetry during nucleus disruption. *Icarus* **166**, 188–194 (2003).
- Hodapp, K. W. et al. Visible and near-infrared spectrophotometry of the Deep Impact ejecta of comet 9P/Tempel 1. *Icarus* **187**, 185–198 (2007).
- Taylor, M. G. T., Altobelli, N., Buratti, B. J. & Choukroun, M. The Rosetta mission orbiter science overview: the comet phase. *Phil. Trans. R. Soc. A* **375**, 20160262 (2017).
- Coradini, A. et al. VIRTIS: an imaging spectrometer for the Rosetta mission. *Space Sci. Rev.* **128**, 529–559 (2007).
- Gicquel, A. et al. Sublimation of icy aggregates in the coma of comet 67P/Churyumov-Gerasimenko detected with the OSIRIS cameras on board Rosetta. *Mon. Not. R. Astron. Soc.* **462**, S57–S66 (2016).
- Keller, H. U. et al. Seasonal mass transfer on the nucleus of comet 67P/Churyumov-Gerasimenko. *Mon. Not. R. Astron. Soc.* **469**, S357–S371 (2017).
- Fornasier, S. Rosetta's comet 67P/Churyumov-Gerasimenko sheds its dusty mantle to reveal its icy nature. *Science* **354**, 1566–1570 (2016).
- Filacchione, G. et al. Exposed water ice on the nucleus of comet 67P/Churyumov-Gerasimenko. *Nature* **529**, 368–372 (2016).
- De Sanctis, M. C., Capria, M. T. & Coradini, A. Thermal evolution model of 67P/Churyumov-Gerasimenko, the new Rosetta target. *Astron. Astrophys.* **444**, 605–614 (2005).
- Capria, M. T. et al. How pristine is the interior of the comet 67P/Churyumov-Gerasimenko? *Mon. Not. R. Astron. Soc.* **469**, S685–S694 (2017).
- Hu, X. et al. Seasonal erosion and restoration of the dust cover on comet 67P/Churyumov-Gerasimenko as observed by OSIRIS onboard Rosetta. *Astron. Astrophys.* **604**, A114 (2017).
- Agarwal, J. et al. Evidence of subsurface energy storage in comet 67P from the outburst of 2016 July 03. *Mon. Not. R. Astron. Soc.* **469**, s606–s625 (2017).
- Bockelée-Morvan, D. et al. Comet 67P outbursts and quiescent coma at 1.3 au from the Sun: dust properties from Rosetta/VIRTIS-H observations. *Mon. Not. R. Astron. Soc.* **469**, S443–S458 (2017).
- Frattini, E. et al. Post-perihelion photometry of dust grains in the coma of 67P Churyumov-Gerasimenko. *Mon. Not. R. Astron. Soc.* **469**, S195–S203 (2017).
- Bardyn, A. et al. Carbon-rich dust in comet 67P/Churyumov-Gerasimenko measured by COSIMA/Rosetta. *Mon. Not. R. Astron. Soc.* **469**, S712–S722 (2017).

Publisher's note Springer Nature remains neutral with regard to jurisdictional claims in published maps and institutional affiliations.

© The Author(s), under exclusive licence to Springer Nature Limited 2020

Methods

VIRTIS dataset

While the scientific objectives of the Rosetta mission^{13,18}, including the study of the dust in the coma, were well-defined before the spacecraft reached 67P, the detailed planning of the scientific payload operations has been a complex and continuously evolving process due to the uncertainties of the cometary environment in which the mission had to operate. A detailed overview of the Rosetta science planning process and challenges is given in ref.³¹. In this context, VIRTIS coma observations were performed from very different viewing and illumination geometries, spacecraft ranges from the nucleus, heliocentric distances and cometary activity levels, resulting in a dataset showing a very variable spatial resolution and signal-to-noise ratio.

While VIRTIS-led targeted observations of the coma have been routinely executed, a large fraction of the VIRTIS dataset consisted of ride-along and serendipitous acquisitions that were acquired while the spacecraft attitude and pointing were controlled by other instruments. For this reason, to maximize the retrieval of information about the dust particles properties, a statistical approach has been applied to the vast VIRTIS dataset with the scope to exploit it in its completeness.

We restrict our analysis to only the VIRTIS-M (imaging channel) visible data covering the 0.25–1.0 μm spectral range with 432 bands and a spectral sampling of less than 2 nm per band. A detailed description of the VIRTIS experiment is provided by ref.¹⁹. In contrast to the VIRTIS-M infrared channel operating within the 1–5 μm spectral range, which ceased operation in May 2015 due to a permanent failure of the cryo-cooler cooling of the infrared channel detector, the visible channel has operated flawlessly for the entire duration of the mission.

For this study, we processed coma data collected during Rosetta's MTP012–MTP028 periods. The time intervals of each medium-term phase (MTP) are listed in Extended Data Table 1. The dataset consists of more than 4,500 hyperspectral cubes of the coma of 67P acquired from a range of distances from the nucleus between 27.8 and 1,462.2 km, resulting in a spatial resolution between 7 and 365 m per pixel, respectively.

Each VIRTIS observation has been calibrated in spectral radiance³² and specific geometry parameters have been calculated for each pixel falling on the coma region and the nucleus. Further details about the VIRTIS data mapping methods are given in ref.⁵. The nucleus solar phase and the spacecraft position and distance in the Cartesian frame centred on the nucleus have been calculated using SPICE kernels³³.

The spectral parameters used in our analysis to study the coma emission are calculated in an annulus defined by a tangent altitude running between $a_{\min} = 1$ km and $a_{\max} = 2.5$ km around the nucleus. This criterion is adopted independently from the nucleus–spacecraft distance and the solar phase angle at the time of the observation. The selection of pixels placed at distances larger than 1 km allows (1) reduction of the contribution of the instrumental stray light coming from the illuminated part of the nucleus and (2) maximization of the coverage across the dataset.

An example of a VIRTIS-M visible image of the coma showing the annulus definition is given in Extended Data Fig. 1 (top panels). This particular image refers to observation MTP019–STP068–V1_00397724286 acquired on 9 August 2015 from a distance of 304 km, resulting in a spatial resolution of 75 m per pixel with an integration time of 16 s per line.

Such a viewing geometry is not very common because the completeness of the annulus over the 360° azimuth (up to distance a_{\max}) is limited by the instrumental field of view (FOV = 3.6°), by the relative distance (d) between the Rosetta spacecraft and the comet's surface, and by the spacecraft off-nadir pointing direction (α). Only when the following condition is verified, VIRTIS-M can acquire the full annulus:

$$\alpha + \arctan\left(\frac{a_{\max} + r}{d}\right) \leq \text{FOV} \quad (1)$$

where $r = 1.74$ km is the average radius of the nucleus³⁴. A similar condition is verified in only 248 observations (marked as red points in Fig. 1a),

corresponding to about 5% of the dataset: as a consequence, integrated radiance and maximum emission wavelength values could be biased by the incompleteness of the annulus on the remaining observations. The average integrated radiance on incomplete annulus observations (black points) appears, in general, higher than on the ones where the annulus is entirely acquired (red points). This happens because VIRTIS is preferentially observing the coma towards the solar direction to maximize the signal-to-noise ratio. Apart from the above limitations, which introduce some scattering in the data points, the value of the integrated radiance is mainly driven by the number of scatterers (dust grains) along the line of sight, rather than by their composition and grain size distribution (which the spectral slopes and the spectral position of the radiance peak depend on).

The overall coma brightness and spectral properties measured by VIRTIS are driven by light scattering on dust particles and are not altered by emissions from gas molecules in the coma. The instrument sensitivity at visible wavelengths, in fact, is not enough to measure gaseous emissions from CN, C₂ and C₃.

Calibration update using stellar observations

With the aim of improving the VIRTIS-M visible response in the 0.25–0.45 μm spectral range, where the standard pipeline suffers large uncertainties due to stray light introduced by the on-ground calibration setup, we applied a radiometric correction based on stellar observations. The average signal derived from Vega (α Lyrae) observations listed in Extended Data Table 2 is used as a reference to correct the standard responsivity. Four observations of Vega acquired with the longest possible integration time, 50 s, were used to retrieve the raw signal above the noise level (about ± 2 data numbers (DN)) estimated on the nearby deep-sky pixels.

Before this step, each observation was dark-level-subtracted and despiked (Extended Data Fig. 2 (top-left panel), showing the signal and sky level for one of the four Vega observations). Owing to the instrumental point spread function and spectral tilt, both described in detail in ref.³⁵, the Vega spectral signal is distributed across 18 spatial pixels and is averaged above these. The four observations were processed in the same way before being further averaged to improve the signal-to-noise ratio. The resulting average Vega signal is shown in Extended Data Fig. 2 (top-right panel). The fractional deviation of the single spectra from the average is about 0.05. The Vega flux in ref.³⁶ is convolved with the VIRTIS Gaussian response (full-width at half-maximum, 2.3 nm) and then by a 4-nm-wide boxcar. The spectra were then placed on an absolute wavelength scale using the centre of Balmer and Paschen intense absorption lines as references and assuming a constant dispersion. The spectral dispersion (in nm) applied is $\lambda(b) = 232.9 + 1.88515 \times b$, with b ranging from 0 to 431, corresponding to the VIRTIS-M number of spectral bands. The resulting relative responsivity derived as the ratio between VIRTIS signal and Vega flux is shown in Extended Data Fig. 2 (bottom-left panel). To further remove residual high-frequency noise due to the low Vega signal, a nine-band running boxcar filter was applied. The response curves were normalized at the value of 58.75 at $\lambda = 0.635 \mu\text{m}$ to allow a direct comparison with the standard pipeline responsivity shown in Extended Data Fig. 2 (bottom-right panel). Within the limits of the low Vega signal in the blue spectral range (less than 40 DN at 0.55 μm), this method allows the retrieval of a better responsivity at shorter wavelengths with respect to the standard pipeline³⁵. As shown by the ratio plot (blue curve), the standard pipeline overestimates the target radiance for wavelengths $\lambda < 0.4 \mu\text{m}$. In the remaining spectral range, the differences are much smaller. As the wavelength of the dust emission spectral radiance peak occurs between 0.45 and 0.55 μm , such an instrument-response correction allows improvement of the retrieval of the left wing of the radiance peak and the spectral slope determinations.

Coma spectral indicators

After averaging the coma signal within the annulus previously defined and applying the updated responsivity function, we calculated four

spectral indicators for each observation. The indicators are as follows. (1) The integrated radiance (I) across the visible spectral range, defined as:

$$I = \frac{\sum_{n=1}^N \int_{0.25\mu\text{m}}^{1\mu\text{m}} R(n, \lambda) d\lambda}{N} \quad (1)$$

where $R(n, \lambda)$ is the spectral radiance measured on the n th pixel of the annulus at wavelength λ and N is the total number of pixels within the annulus area. (2) The wavelength of maximum emission of the radiance (λ_{max}) measured on a fourth-degree fit on the average spectral radiance calculated on the annulus.

After converting spectral radiance to irradiance/solar flux (I/F), we calculated the two spectral slopes following ref. ⁵. These are: (3) 0.4–0.5 μm spectral slope on I/F ; and (4) 0.5–0.8 μm spectral slope on I/F . The two spectral slopes are calculated as the angular coefficient of the best linear fit in the ranges 0.4–0.5 and 0.5–0.8 μm after having normalized I/F at 0.5 μm . The determination of the spectral indicators follows the scheme shown in Extended Data Fig. 1 (bottom panels).

Spectral indicators depend on illumination geometries and the spacecraft–nucleus distance: as a consequence of the demanding mission scenario, complex orbits, including terminator, icosahedron, flybys and far excursions, have been flown³¹, resulting in a wide range of distances and solar phases. The correlation between the integrated radiance I and distance is shown in Extended Data Fig. 3, where VIRTIS-M measurements are co-located with Rosetta’s position and solar phase angle with respect to the comet nucleus along the flight trajectory.

Temporal evolution of the coma colour

The integrated radiance (I) time series (Fig. 1a) shows an increase in the coma’s brightness starting from January 2015 (MTP012, heliocentric distance 2.55 AU) to perihelion passage (MTP019, 1.24 AU, August 2015). Owing to the characteristics of Rosetta’s orbit around the nucleus and the different observation strategies implemented during the mission, the completeness of the annulus region on the VIRTIS dataset is reached on only a limited number of observations, marked as red points in Fig. 1a. For the majority of the remaining observations (black points), partial coverage of the annulus is achieved. Notwithstanding the relative scatters of the data introduced by the variability of the observing conditions, some clear trends are identified. A local maximum, $25 \leq I \leq 30 \text{ W m}^{-2} \text{ sr}^{-1}$, is measured about one month after perihelion. Two additional intensity peaks are measured at the end of August and September 2015, when a maximum intensity of about $50 \text{ W m}^{-2} \text{ sr}^{-1}$ is reached. These peaks are caused by energetic cometary activity—two outbursts observed by VIRTIS on 13–14 September 2015 are reported by refs. ^{28,37}—but appear also to be strongly correlated with the peculiar viewing geometry and spacecraft position with respect to the nucleus: in fact, at the time of these observations, Rosetta was performing far-nucleus excursions, orbiting at greater distances than usual from the nucleus, up to 450 and 1,462 km, respectively. As a consequence of the increased distance from the nucleus, VIRTIS-M has recorded higher radiances boosted by the larger column density of dust particles along the line of sight and by the maximum activity occurring immediately after perihelion. After this period, the integrated radiance drops rapidly from MTP021 to MTP024 where an average value of $5 \text{ W m}^{-2} \text{ sr}^{-1}$ is reached. The maximum integrated radiance measured in MTP020 and MTP021 is about a factor of 10 more intense than the average value of $5 \text{ W m}^{-2} \text{ sr}^{-1}$ measured when the comet was far from the Sun (greater than 2 AU) on both inbound and outbound legs of the orbit. With the exclusion of the two peaks, a similar asymmetric, or cusp-like trend with a maximum occurring about one month after perihelion, has been measured by other Rosetta’s instruments for the water production rate, which is associated with the ejection of the dust³. Apart from the greater column density, we have clues that a larger particle albedo could contribute to the increase of the integrated radiance: according

to ref. ⁴, the albedo of the dust particles increases up to 20% near perihelion for observations acquired at a 90° solar phase angle. Similar albedo changes could be the result of a different composition of the dominant grain population in the coma along the orbit, as discussed in the main text.

The time series of the wavelength of maximum emission (λ_{max}) (Fig. 1c) shows a cusp-like trend starting from low values dispersed around $\lambda_{\text{max}} = 0.45 \mu\text{m}$ on January 2015 (MTP012) on the inbound leg of 67P trajectory to $\lambda_{\text{max}} > 0.5 \mu\text{m}$ during perihelion passage (MTP019). Moving along the outbound leg of the orbit, the wavelength of maximum emission shifts progressively towards shorter wavelengths, reaching again $\lambda_{\text{max}} = 0.45 \mu\text{m}$ in mid-May 2016 (MTP028). Whereas λ_{max} and integrated radiance time series show a similar time trend, spectral slopes time series (Fig. 1b, d) are characterized by a different evolution: at the two extremes of the time series, both 0.4–0.5 μm and 0.5–0.8 μm slopes are almost neutral whereas at perihelion they reach values dispersed at 5 and 3 μm^{-1} , respectively. The visible colours of the coma show a systematic reddening before perihelion passage and a progressive blueing after it. The concurrent variations occurring on all spectral indicator time series point to a change in the dust grain composition and grain size distribution with the heliocentric distance.

Temporal evolution of the nucleus colour

When observed at a global scale, 67P surface dust appears very dark (geometric visible albedo 6.2%; ref. ³⁸) and dehydrated, with an average water-ice fraction of about 1% dispersed in submicrometre grains^{39,40}. The residual water-ice content, if present, on the dust grains ejected from the surface undergoes rapid sublimation once the grain is lifted²⁰. So far, infrared spectroscopic observations have confirmed the presence of only two ices on the surface of 67P nucleus: water ice^{23,41} and carbon dioxide⁴².

The low thermal capacity of the dust ($700 \text{ J kg}^{-1} \text{ K}^{-1}$) and the high solar flux can rapidly increase the temperature of the grains causing the sublimation of the volatiles. A colour temperature as high as 630 K is measured on dust grains during outbursts²⁸ and in the 260–320 K range on quiescent coma⁴. Furthermore, the grains observed by Rosetta’s dust instruments appear dehydrated^{30,43}. This probably happens because the instruments aboard the spacecraft are not kept at cryogenic temperatures, allowing the dispersion of the volatile fraction of the grains after their collection. Besides dehydration, grain size distribution also plays a role in the changes of the visible colours (see ‘Modelling dust grain composition and size distribution in the coma’).

During the pre-perihelion phase, the nucleus’ surface shows a progressive blueing until one month after perihelion when the minimum slope is reached in MTP020 (Fig. 2). In this phase, the gas activity removes the dust from the surface with greater efficiency, resulting in the exposure of more pristine subsurface material enriched in ices^{5,6,22}. This trend is interrupted after the perihelion passage when a progressive surface reddening is observed. Along the outbound trajectory, the gaseous activity progressively settles, resulting in the accumulation of dehydrated (red) dust on the surface. This appears to be a general mechanism, occurring on the majority of the nucleus surface, as shown in Fig. 2, where the average 0.5–0.8 μm slope is shown for twelve $30 \text{ m} \times 30 \text{ m}$ -wide control areas at one-month time resolution. These control areas, selected between latitude +45.5° and –34.5°, are the ones that have been observed in daylight by VIRTIS during the entire duration of the mission, allowing us to follow the seasonal colour cycle developing on the nucleus.

Dust-scattering simulations

The simulations are computed following the Bohren–Huffman Mie scattering code⁴⁴ to calculate scattering and absorption by a homogenous isotropic sphere. The method relies on the following assumptions. (1) Single-scattering approximation, for example, the solar photons interact with only one particle before reaching the observer. Such a

hypothesis is reasonable for the annulus region considered in this study, where the optical depth is small. (2) Polydisperse spherical grain size distributions with radii of 0.10–0.99 μm (90 bins, 0.01 μm per bin), 1.0–9.9 μm (90 bins, 0.1 μm per bin) and 10–50 μm (40 bins, 1 μm per bin). (3) Five different grain compositions are simulated: water ice (optical constants from ref. ⁴⁵), organic material⁴⁶, troilite⁴⁵, amorphous carbon⁴⁷ and magnesium silicate⁴⁸. These endmembers are representative of the cometary nuclei composition, which is made up of a macromolecular assemblage in which various organic components (both aromatic and aliphatic), minerals (including silicates, iron sulphides like pyrrhotite and/or troilite, and possibly ammoniated salt) and ices are mixed together⁴⁹. (4) Spectral simulations are performed at 27 wavelengths within the 0.35–1.0 μm spectral range. (5) Scattering angle θ ($= 180^\circ - g$, where g is the solar phase angle) is computed at a step of 1° from 55° to 155° and then averaged on 4° bins to match the VIRTIS FOV (3.66°).

Following ref. ⁵⁰, the single scattering intensity is given by:

$$I(\lambda) = S(\lambda)n_{\text{col}}(\rho)\sigma q(\lambda) \frac{p(g, \lambda)}{4\pi} \quad (2)$$

where $S(\lambda)$ is the solar flux⁵¹ scaled at the comet's heliocentric distance, n_{col} is the dust column density calculated along the line of sight from an observer placed at distance ρ from the nucleus, σ is the grain geometrical cross-section, $q(\lambda)$ is the scattering efficiency of a single particle and $p(g, \lambda)$ is the scattering phase function calculated at phase g . Rather than modelling the absolute value of the intensity, we limit here our analysis to the changes occurring in the spectral response of the average radiance emitted from the dust. In particular, we focus on the changes of the wavelength of the maximum emission (Fig. 1c) and 0.5–0.8 μm spectral slope (Fig. 1d) observed at different heliocentric distances. To achieve this goal, we calculated the spectral radiance factor, $I(\lambda)$ expressed in arbitrary units, derived from Eq. (2) by removing the factors depending on the dust grain distribution and properties:

$$I(\lambda, g) \propto S(\lambda)q(\lambda) \frac{p(g, \lambda)}{4\pi} \quad (3)$$

The phase functions show scattering characteristics depending on composition and grain sizes: as a general rule, transparent grains, like water ice, are characterized by a very intense and collimated forward-scattering peak and complex resonance peaks at intermediate phase angles. Opaque materials, like troilite, show an almost isotropic scattering function. Semi-transparent particles, like ice tholins, have an intermediate behaviour with a prevalence of backscattering response. Grain size plays a fundamental role in the scattering mechanism: in the Rayleigh regime (particle size much smaller than the wavelength), light is equally forward- and backscattered while in the geometric regime (particle size much larger than the wavelength), backscattering dominates.

Fixing composition and grain size, the corresponding phase functions at the 27 visible wavelengths allow the derivation of the spectral radiance according to Eq. (3).

While $p(g, \lambda)$ has a smooth response in the Rayleigh and in the geometric scattering regimes, the simulations, in general, show more fluctuations occurring for certain combinations of composition, grain size and θ angle when the grain sizes are comparable to the wavelength, for example, at about 1 μm . To mitigate this effect, we computed simulations for $25^\circ \leq g \leq 125^\circ$, corresponding to scattering angles of $55^\circ \leq \theta \leq 155^\circ$, at steps of 1° and then averaged the angular response of $p(g, \lambda)$ on 4° bins, similar to the VIRTIS FOV. Similarly, the $p(g)$ was computed for single grain radius (0.10–0.99 μm (90 bins, 0.01 μm per bin), 1.0–9.9 μm (90 bins, 0.1 μm per bin) and 10–50 μm (40 bins, 1 μm per bin)) and then averaged for each of the three families. Following this method, the $I(\lambda, g)$ (from Eq. (3)) was derived for each composition and

size distribution. The λ_{max} and, after conversion in I/F , the 0.5–0.8 μm spectral slope were derived from the simulated $I(\lambda, g)$. The corresponding values are shown in Figs. 3, 4, respectively.

Modelling dust grain composition and size distribution in the coma

To disentangle the viewing and illumination geometry effects from particles' physical properties and to provide a more quantitative assessment of the changes observed in the λ_{max} time series, the light scattering on grains of different composition and radius was simulated. Optical and in situ measurements of the dust grain distribution in the 67P coma by Rosetta's instruments have revealed that the particles lie mainly within the 0.1 μm –1 mm diameter range⁵². For particles smaller than 1 mm, the dust size distribution follows a power-law distribution with a coefficient varying between -2 for heliocentric distances beyond 2 AU and -3.7 at perihelion. Conversely, large grains (diameter greater than 1 mm) show a much steeper distribution with a coefficient of -4 (ref. ⁵³). As small grains are the predominant population, in our analysis we preferentially model the spectral behaviour of small (radius less than 50 μm), compact grains. A similar grain size range has been also used by refs. ^{28,37} to model dust optical properties at infrared wavelengths and by ref. ²⁰ to study thermal evolution and depletion of ice in dust aggregates along jets. The VIRTIS data are interpreted through the Mie theory, which can simulate the scattering properties of spherical grains of radius R and homogeneous composition having $x = (2\pi R/\lambda) < 1,000$. Such a limit corresponds to a maximum grain radius $R = 50 \mu\text{m}$ in the visible spectral range (wavelength $0.35 \leq \lambda \leq 1.0 \mu\text{m}$). To simulate the spectral response of larger grains, including fluffy aggregates^{7,54}, it is necessary to use a geometric optics approximation⁵⁵, which is beyond the scope of this work.

The changes occurring in the spectral radiance scattered by spherical grains of different composition and grain size distribution as a function of the phase angle (g) are calculated for homogeneous particles made of possible cometary material endmembers, including water ice, organic ice tholin, troilite, amorphous carbon and magnesium silicate. For a given composition and phase angle, the single particle phase function $p(g, \lambda)$ modulates the intensity of the scattered spectral radiance.

The theoretical trends of λ_{max} as a function of the scattering angle $\theta = 180^\circ - g$ for particles of different composition and three grain size distributions (radius 0.10–0.99 μm , 1.0–9.9 μm and 10–50 μm) considered in this study, are shown in Fig. 3. In the same figure, we show the distribution of λ_{max} as measured from VIRTIS observations (Fig. 3f) selected during six MTP periods encompassing pre-perihelion (MTP015 and MTP016), perihelion (MTP020 and MTP021) and post-perihelion (MTP027 and MTP028) orbital phases. These periods are chosen because they offer the widest spread in scattering angle necessary to discriminate among different compositions and grain size distributions. Our analysis shows that, with the exception of transparent grains, for example, water ice and organic ice tholin, the response of opaque materials like amorphous carbon (Fig. 3a) and troilite (Fig. 3d) are characterized by a constant λ_{max} at about 0.5 μm for the intermediate (1.0–9.9 μm) and large (10–50 μm) grain size distributions across the $60^\circ \leq \theta \leq 150^\circ$ scattering angle range explored by VIRTIS. These grains are therefore not matching the observed distribution of the λ_{max} . Conversely, opaque-material submicrometre grains show a significant shift of the λ_{max} towards the red range, especially for $\theta \leq 120^\circ$.

Submicrometre grains made of magnesium silicate (Fig. 3b) show a linear increasing trend of λ_{max} from 0.56 μm at $\theta = 60^\circ$ to 0.63 μm at $\theta = 150^\circ$, which is not compatible with VIRTIS data. In contrast, the λ_{max} of grains with radii larger than 1 μm is dispersed around 0.55 μm , a value too red to reproduce VIRTIS data at $\theta > 100^\circ$ and too blue for $\theta < 100^\circ$.

Water-ice grains (Fig. 3e) offer the only solution matching VIRTIS data taken during the pre- (MTP015 and MTP016) and post-perihelion periods (MTP027 and MTP028) at scattering angles $\theta > 100^\circ$. During these phases, VIRTIS data are dispersed at $\lambda_{\text{max}} < 0.5 \mu\text{m}$, a behaviour

compatible with only the three water-ice grain-size distributions we have simulated.

Apart water ice, organic material grains (Fig. 3c) are the second end-member showing spectral similarities compatible with 67P particles: the 1–10 μm and 10–50 μm grain-size responses are in fact characterized by a linear decrease of λ_{max} from $\theta = 60^\circ$ to 120° , making them compatible with observations acquired during perihelion and post-perihelion periods. In contrast, submicrometre grains show an extreme red colour across the entire range of scattering angles: having $\lambda_{\text{max}} \geq 0.65 \mu\text{m}$, they are marginally compatible only with VIRTIS observations taken at low θ angles. If one assumes that during one month, for example, during the duration of one MTP period, the dominant composition and grain size is preserved, then the VIRTIS measurements taken during MTP028 at $\theta > 130^\circ$ could be compatible not only with water ice but also with large (10–50 μm) organic material grains. As shown in Fig. 3a, amorphous carbon submicrometre-size (0.1–0.9 μm) grains are characterized by a reddening of λ_{max} for $\theta < 90^\circ$, similar to VIRTIS but with absolute values too low to exactly match the observations. Instead, the match is compatible for $90^\circ < \theta < 120^\circ$, making submicrometre amorphous carbon grains a good interloper between water-ice and organic grains. Finally, magnesium silicate (Fig. 3b) and troilite (Fig. 3d) submicrometre grains show λ_{max} trends at low scattering angles not compatible with VIRTIS data.

Composition and grain size distribution of the dust particles were further analysed through the 0.5–0.8 μm spectral slope (Fig. 4) derived from VIRTIS data, which shows a peaked distribution at $\theta = 100$ – 110° (Fig. 4f) occurring in perihelion (MTP020 and MTP021) and post perihelion (MTP028) sequences. In our simulations, a similar behaviour is compatible with submicrometre-size grains made of organic matter (black points in Fig. 4e) or with greater than 1 μm water-ice grains (blue and red points in Fig. 4d). The absolute value of the slope on the peak (about $3 \mu\text{m}^{-1}$) measured at perihelion (MTP020, cyan points) is similar to theoretical values for organic matter. Being transparent, water-ice particles are characterized by a peculiar behaviour: submicrometre grains show a blue colour response (negative slope, black points in Fig. 4d) not compatible with any VIRTIS observation, whereas large grains (blue and red points) are neutral to moderately red and could contribute to the VIRTIS observed slope at any scattering angle. Opaque grains with sizes greater than 1 μm show an almost constant neutral to moderately red ($0.5 \mu\text{m}^{-1}$) slope within the entire scattering angle range (see red and blue points for amorphous carbon in Fig. 4a and troilite in Fig. 4b). We remark that while the λ_{max} trends of magnesium silicate (Fig. 3b) grains are not compatible with VIRTIS data, their spectral slopes values (Fig. 4c) for radii greater than 1 μm are remarkably similar for measurements taken during the post-perihelion period.

Extended Data Table 3 shows the compatibility scheme of the λ_{max} and 0.5–0.8 μm spectral slope values for the different composition endmembers, grain radius and scattering angle compared with the VIRTIS data.

Data availability

The VIRTIS calibrated data are publicly available through the European Space Agency's Planetary Science Archive website (<https://archives.esac.esa.int/psa/>).

31. Vallat, C. et al. The science planning process on the Rosetta mission. *Acta Astronaut.* **133**, 244–257 (2017).
32. Filacchione, G. et al. On-ground characterization of Rosetta/VIRTIS-M. II. Spatial and radiometric calibrations. *Rev. Sci. Instrum.* **77**, 103106–103106-9 (2006).

33. Acton, C. H. Ancillary data services of NASA's Navigation and Ancillary Information Facility. *Planet. Space Sci.* **44**, 65–70 (1996).
34. Jorda, L. et al. The global shape, density and rotation of comet 67P/Churyumov-Gerasimenko from preperihelion Rosetta/OSIRIS observations. *Icarus* **277**, 257–278 (2016).
35. Filacchione, G. Calibrazioni a terra e prestazioni in volo di spettrometri ad immagine nel visibile e nel vicino infrarosso per l'esplorazione planetaria. PhD thesis, Università di Napoli Federico (2006).
36. Bohlin, R. C. & Gilliland, R. L. Hubble Space Telescope absolute spectrophotometry of Vega from the far-ultraviolet to the infrared. *Astron. J.* **127**, 3508–3515 (2004).
37. Rinaldi, G. et al. Summer outbursts in the coma of comet 67P/Churyumov-Gerasimenko as observed by Rosetta-VIRTIS. *Mon. Not. R. Astron. Soc.* **481**, 1235–1250 (2018).
38. Ciarniello, M. et al. Photometric properties of comet 67P/Churyumov-Gerasimenko from VIRTIS-M onboard Rosetta. *Astron. Astrophys.* **583**, A31 (2015).
39. Capaccioni, F. et al. The organic-rich surface of comet 67P/Churyumov-Gerasimenko as seen by VIRTIS/Rosetta. *Science* **347**, aaa0628 (2015).
40. Raponi, A. et al. The temporal evolution of exposed water ice-rich areas on the surface of 67P/Churyumov-Gerasimenko: spectral analysis. *Mon. Not. R. Astron. Soc.* **462**, S476–S490 (2016).
41. De Sanctis, M. C. et al. The diurnal cycle of water ice on comet 67P/Churyumov-Gerasimenko. *Nature* **525**, 500–503 (2015).
42. Filacchione, G. et al. Seasonal exposure of carbon dioxide ice on the nucleus of comet 67P/Churyumov-Gerasimenko. *Science* **354**, 1563–1566 (2016).
43. Hilchenbach, M. et al. Comet 67P/Churyumov-Gerasimenko: close-up on dust particle fragments. *Astrophys. J. Lett.* **816**, L32 (2016).
44. Bohren, C. F. & Huffman, D. R. *Absorption and Scattering of Light by Small Particles* (Wiley, 1983).
45. Pollack, J. B. et al. Composition and radiative properties of grains in molecular clouds and accretion disks. *Astrophys. J.* **421**, 615–639 (1994).
46. Cuzzi, J. N., Estrada, P. R. & Sanford, D. S. Utilitarian opacity model for aggregate particles in protoplanetary nebulae and exoplanet atmospheres. *Astrophys. J. Suppl. Ser.* **210**, 21 (2014).
47. Zubko, V. G. et al. Optical constants of cosmic carbon analogue grains—I. Simulation of clustering by a modified continuous distribution of ellipsoids. *Mon. Not. R. Astron. Soc.* **282**, 1321–1329 (1996).
48. Dorschner, J. et al. Steps towards interstellar silicate mineralogy. II. Study of Mg-Fe-silicate glasses of variable composition. *Astron. Astrophys.* **300**, 503–520 (1995).
49. Filacchione, G. et al. Comet 67P/CG nucleus composition and comparison to other comets. *Space Sci. Rev.* **215**, 19 (2019).
50. Fink, U. & Rinaldi, G. Coma dust scattering concepts applied to the Rosetta mission. *Icarus* **257**, 9–22 (2015).
51. Kurucz, R. L. Synthetic infrared spectra. In *Proc. IAU Symposium 154, Infrared Solar Physics* (eds Rabin, D. M. et al.) 523 (Kluwer, 1994).
52. Rotundi, A. Dust measurements in the coma of comet 67P/Churyumov-Gerasimenko inbound to the Sun. *Science* **347**, aaa3905 (2015).
53. Fulle, M. et al. Evolution of the dust size distribution of comet 67P/Churyumov-Gerasimenko from 2.2 au to perihelion. *Astrophys. J.* **821**, 19 (2016).
54. Fulle, M. et al. Density and charge of pristine fluffy particles from comet 67P/Churyumov-Gerasimenko. *Astrophys. J. Lett.* **802**, L12 (2015).
55. Grynko, Y. & Shkuratov, Y. G. in *Light Scattering Reviews 3* (ed. Kokhanovsky, A. A.) Ch. 9 (Springer Praxis, 2008).

Acknowledgements The authors thank the following institutions and agencies that supported this work: Italian Space Agency (ASI-Italy), Centre National d'Etudes Spatiales (CNES-France), Deutsches Zentrum für Luft-und Raumfahrt (DLR-Germany). VIRTIS was built by a consortium from Italy, France and Germany, under the scientific responsibility of IAPS, Istituto di Astrofisica e Planetologia Spaziali of INAF, Rome, which lead also the scientific operations. The VIRTIS instrument development for ESA has been funded and managed by ASI (Italy), with contributions from Observatoire de Meudon (France) financed by CNES and from DLR (Germany). The VIRTIS instrument industrial prime contractor was former Officine Galileo, now Leonardo Company, in Campi Bisenzio, Florence, Italy. This research has made use of NASA's Astrophysics Data System.

Author contributions The paper is a collective effort by the VIRTIS dust working group. F.G. as the main author of the paper calibrated, processed and interpreted VIRTIS data. F.C. as the VIRTIS principal investigator managed the experiment; M.C., A.R. and G.R. supported the Mie scattering calculations and data processing; F.C. and D.B.-M. planned 67P coma observations by VIRTIS; F.C. and G.F. planned the 67P nucleus observations by VIRTIS; S.E. provided geometry files for coma and nucleus observations; all authors, including M.C.D.C., G.A., V.M., M.F., A.L. and S.M., have contributed to the discussion of the results.

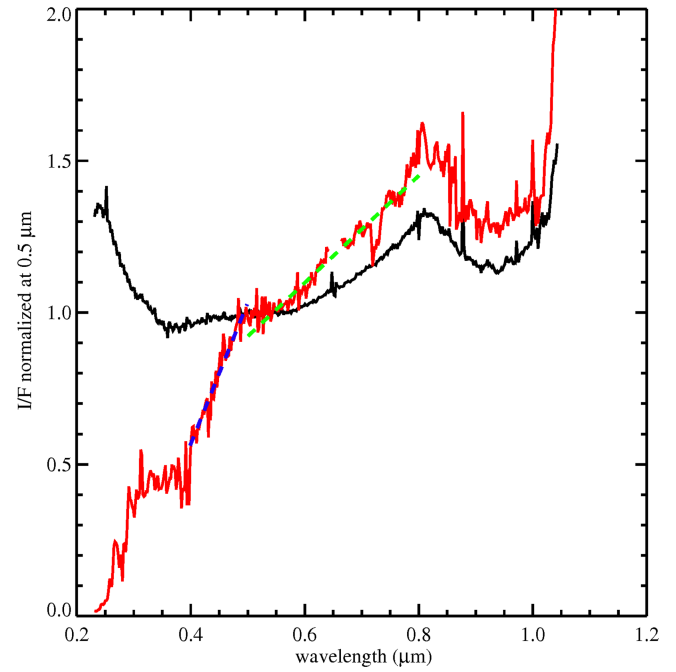
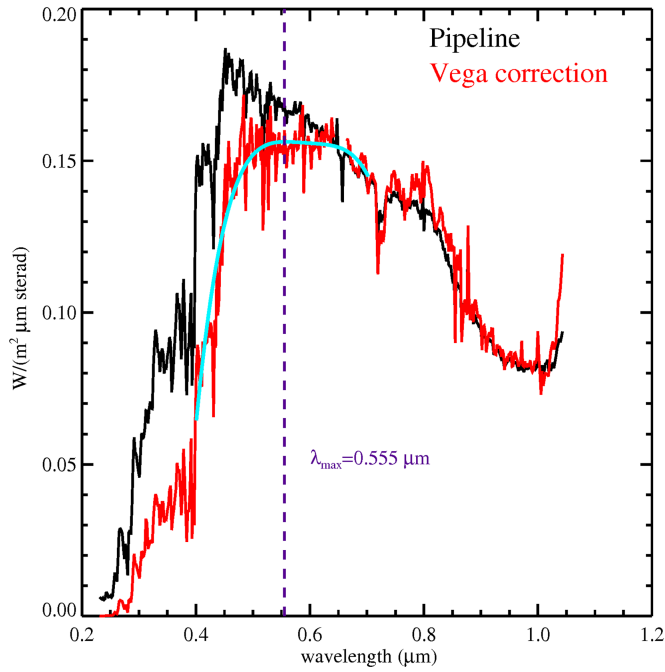
Competing interests The authors declare no competing interests.

Additional information

Correspondence and requests for materials should be addressed to G.F.

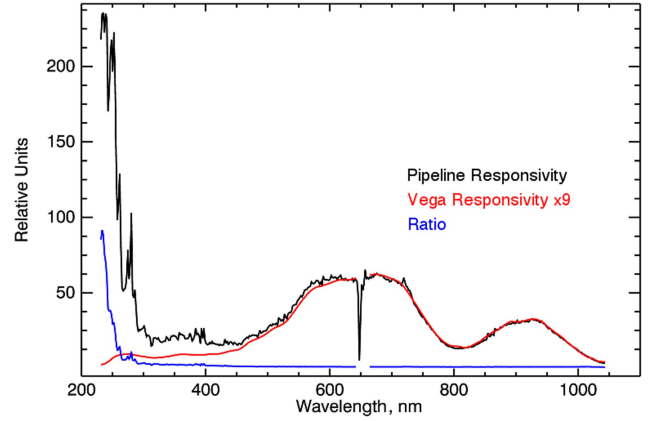
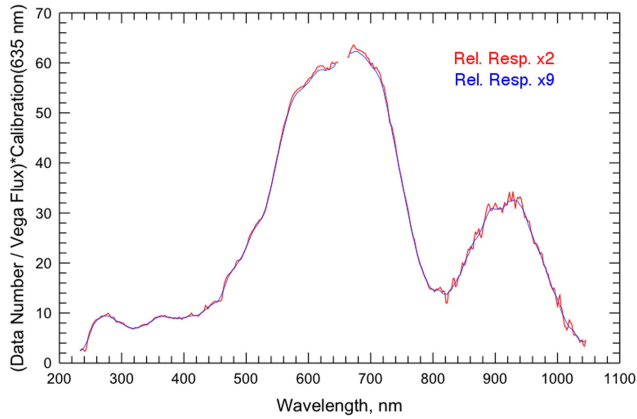
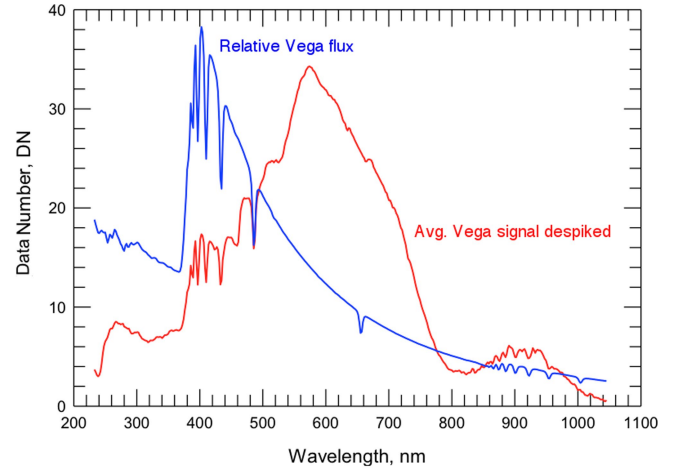
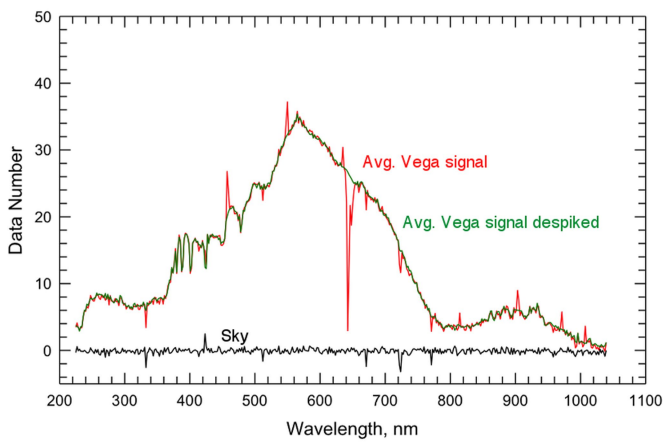
Peer review information Nature thanks Evgenij S. Zubko and the other, anonymous, reviewer(s) for their contribution to the peer review of this work.

Reprints and permissions information is available at <http://www.nature.com/reprints>.



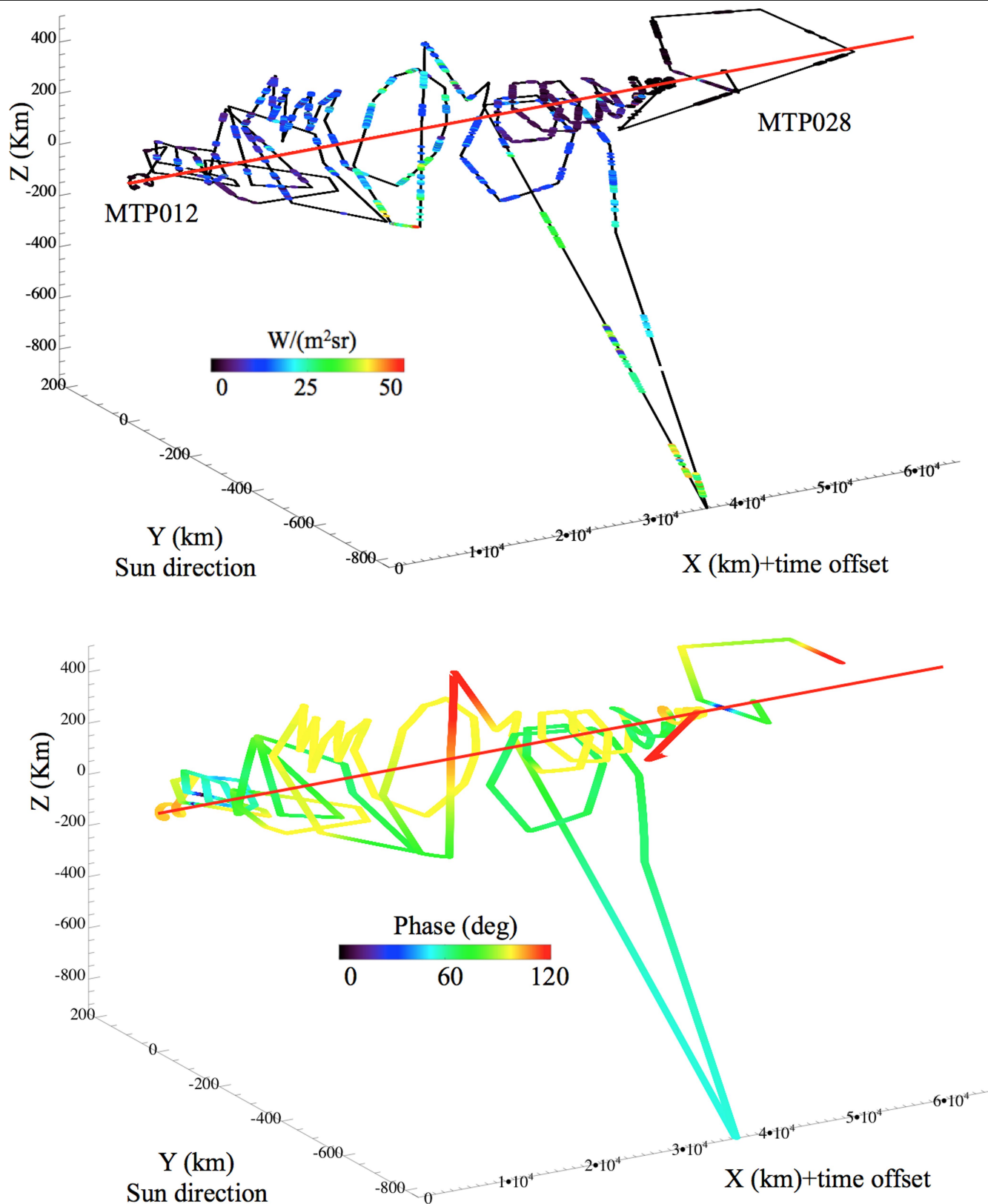
Extended Data Fig. 1 | Example of a typical VIRTIS-M observation of 67P nucleus and coma. Top left: visible colours RGB = (0.7, 0.55, 0.44 μm) image, stretched to saturate the nucleus and enhance the visibility of jets in the coma. Top right: tangent altitude image where the green mask corresponds to the annulus containing all pixels with a tangent altitude between 1 and 2.5 km from the limb. Bottom left: average radiance spectra as derived from official

pipeline (black curve) and after correction with Vega data (red curve). The fourth-degree polynomial fit to the corrected radiance is shown (cyan curve). The retrieved maximum emission wavelength on the fit is indicated by the magenta dashed line. Bottom right: corresponding I/F spectra normalized at $0.5 \mu m$. The best-fitting slopes in the $0.4-0.5$ and $0.5-0.8 \mu m$ ranges are indicated by blue and green dashed lines, respectively.



Extended Data Fig. 2 | Vega star signal and derived VIRTIS responsivity. Top left: average spectrum of Vega, in DN, from observation V1_00402035638.QUB (red curve) and spectrum corrected for dark current, despiked and filter notch removed (green curve). Note the correlation of negative spikes in the Vega and average sky spectrum (black curve). Owing to the instrumental point spread function and spectral tilt, the signal is an average taken from 18 pixels. Top right: average spectrum of Vega derived from the four observations listed in Extended Data Table 2 after having applied a processing similar to the one

shown in the previous plot. The curve is averaged with a two-point running boxcar filter. The Vega flux³⁶ is shown in relative units (blue curve). Bottom left: VIRTIS responsivity derived from Vega signal averaged with a two-point running boxcar filter (red curve) and nine points (blue curve) after normalization at 0.635 μm above the standard responsivity value. Bottom right: comparison between standard pipeline (black curve) and Vega responsivities with a nine-point running boxcar filter (red curve). The ratio between the two responses is the blue curve.



Extended Data Fig. 3 | Rosetta spacecraft three-dimensional trajectory and solar phase angle variations with time. Top: Rosetta trajectory in the 67P XYZ reference frame. Points along the X axis are shown starting from Rosetta's position at 2015-01-13T23:28:53 (MTP012) with an increment of 1 km every 20 min to improve visualization. The Y axis is oriented towards the Sun and the

Z axis is perpendicular to the orbital plane. The red line indicates the position of the nucleus along the X axis. The integrated radiance as measured on each observation is reported according to the colour scale. Bottom: variation of the solar phase angle (Sun–nucleus centre–Rosetta) during the mission.

Article

Extended Data Table 1 | Rosetta's calendar MTP periods dates and heliocentric distance

Period	Start Time	End Time	Heliocentric distance (AU)
MTP012	2015-01-13T23:28:53	2015-02-10T23:23:53	2.552-2.344
MTP013	2015-02-10T23:23:53	2015-03-10T23:23:53	2.344-2.130
MTP014	2015-03-10T23:23:53	2015-04-08T23:23:53	2.130-1.967
MTP015	2015-04-08T23:23:53	2015-05-05T23:23:53	1.967-1.703
MTP016	2015-05-05T23:23:53	2015-06-02T23:23:53	1.703-1.508
MTP017	2015-06-02T23:23:53	2015-06-30T23:23:53	1.508-1.350
MTP018	2015-06-30T23:23:53	2015-07-28T23:23:52	1.350-1.257
MTP019	2015-07-28T23:23:52	2015-08-25T23:23:52	1.257-1.253
MTP020	2015-08-25T23:23:52	2015-09-22T23:23:52	1.253-1.340
MTP021	2015-09-22T23:23:52	2015-10-20T23:23:52	1.340-1.494
MTP022	2015-10-20T23:23:52	2015-11-17T23:23:52	1.494-1.686
MTP023	2015-11-17T23:23:52	2015-12-15T23:28:52	1.686-1.897
MTP024	2015-12-15T23:28:52	2016-01-12T23:28:52	1.897-2.113
MTP025	2016-01-12T23:28:52	2016-02-09T23:28:52	2.113-2.327
MTP026	2016-02-09T23:28:52	2016-03-08T23:28:52	2.327-2.536
MTP027	2016-03-08T23:28:52	2016-04-05T23:28:52	2.536-2.738
MTP028	2016-04-05T23:28:52	2016-05-03T23:27:51	2.738-2.933

Extended Data Table 2 | List of VIRTIS observations of the Vega star

Observation	Start Time	End Time	(Band, Sample, Line)	Int. Time (s)
V1_00402035638.QUB	2015-09-28T04:35:17.781	2015-09-28T05:04:11.405	(432,256,29)	50
V1_00403369562.QUB	2015-10-13T15:07:22.178	2015-10-13T15:38:15.817	(432,256,31)	50
V1_00403848118.QUB	2015-10-19T04:03:18.373	2015-10-19T04:34:12.013	(432,256,31)	50
V1_00406049718.QUB	2015-11-13T15:36:39.065	2015-11-13T16:03:32.757	(432,256,27)	50

Extended Data Table 3 | Summary of spectral indicator compatibility

Composition	Grain radius (µm)	Scattering Angle (deg)									
		60	70	80	90	100	110	120	130	140	150
Amorphous Carbon	0.10-0.99										
	1.0-9.9										
	10-50										
Mg-silicate	0.10-0.99										
	1.0-9.9										
	10-50										
Organics	0.10-0.99										
	1.0-9.9										
	10-50										
Troilite	0.10-0.99										
	1.0-9.9										
	10-50										
Water Ice	0.10-0.99										
	1.0-9.9										
	10-50										

Compatible (<1 stdev)

Marginal compatible (<2 stdev)

Not compatible (>2 stdev)

N/A coverage

Pre-Perihelion

Perihelion

Post-Perihelion

0.5-0.8 µm spectral slope

λ_{MAX}

The table shows the compatibility of spectral indicators (λ_{max} , 0.5–0.8 µm spectral slopes) between VIRTIS observations and Mie scattering simulations for a given composition, grain radius range and scattering angle. The compatibility between observations and scattering simulations is colour coded according to the key shown on the top right. Each cell is divided in four fields showing λ_{max} and to 0.5–0.8 µm slope values during pre-perihelion, perihelion and post-perihelion epochs (bottom right key).

Reproduced with permission of copyright owner. Further reproduction prohibited without permission.